Heliyon 8 (2022) e10532

Contents lists available at ScienceDirect

Heliyon

journal homepage: www.cell.com/heliyon

Research article

An optofluidic Bragg fiber sensor for estimating adulterants in a temperature-dependent molar fraction of hydrated mono-alcohol fuels

Nitesh K. Chourasia [a], Narendra Bihari [b,c], Ritesh Kumar Chourasia [b,*]

[a] School of Physical Sciences, Jawaharlal Nehru University, New Delhi, 110067, India
[b] Post Graduate Department of Physics, Samastipur College, Samastipur, 848134 [1], India
[c] University Department of Physics, Lalit Narayan Mithila University, Darbhanga, 846004, India

ARTICLE INFO

Keywords:
Bragg fiber sensor
Adulteration
Mono-alcohols fuel
Henkel formalism
Defect mode
Sensitivity
Detection accuracy
Quality parameter

ABSTRACT

Since, chemically complex environments, the aroma has been a difficult task so far. Therefore, in the present communication, an optofluidic Bragg fiber artificial nose for perceiving the temperature-functional molar fraction of an adulterated binary composition of hydrated mono-alcohols is optimized and reported. The task is theoretically predicted over an optofluidic Bragg fiber sensor having geometrical defects by creating an asymmetry in mid of periodic cylindrical Bragg reflectors. In a cylindrical coordinate system, Henkel function (HF) and transfer matrix technique (TMT) are used to simulate a multilayer concentric hollow-core Bragg fiber (HCBF). The variation in refractive index (RI) of the adulterated binary mono-alcohol fuel is connected to the temperature-functional molar concentration, which is again anticipated by making use of several models, including the most suitable Dale-Gladstone, Lorentz-Lorenz, etc. A prominent sensing signal of which has the full width at half maximum (FWHM) equal to 0.1 nm is observed in the examined photonic bandgap (PBG). The signal is responsive to fluctuations in optofluidic core RI in the vicinity of a structural defect layer. The suggested sensor's temperature-dependent maximum sensitivity (due to varied weather circumstances) for ethanol fuel rather than methanol fuel is 1057.32 nm/RIU. Furthermore, the surface plasmon-based static temperature sensor is compared. Due to the smallest FWHM of output signal around 0.1 nm, other sensing performance metrics such as detection accuracy and quality parameters are also enhanced in the proposed sensor device.

1. Introduction

Adulteration is described as the improper or unlawful inclusion of foreign material into a base fuel or similar substance, causing the product to fail to meet the product's criteria and specifications. Adulterants are exogenous compounds that, when added, modify and impair the quality of essential transportation fuels. When items of equal quality have varying costs or buyers lack adequate means to discriminate between identical objects of multiple standards, nefarious operators will try to benefit illegally from the situation. Fuel adulteration is one of the primary abuses in the retail industry, along with under-dispensing items to clients. These tactics lead to losses in various areas, including engine failure and deteriorating air quality. Fuel tax evasion also affects federal revenue. Consumer losses result from the under-distribution of supplies. Though we are all aware, biomass-based fuels have tremendous energy potential, and one of the key advantages is that they reduce greenhouse gas emissions. These fuels are a sustainable fuel source that will eventually lessen reliance on ex-submerged biomass like petroleum while also assisting in developing a strategic reserve [1, 2]. Monoalcohals, whether pure or hydrated, are a kind of biomass fuel commonly employed as an energy source in cosmetics, the pharmaceutical industry, etc. [3]. The quantity of diesel, petrol, gasoline, and other fossil fuels is considered constrained in the perspective of energy fuels. Mono-alcohol can be environmentally benign biofuels that may be used instead of diesel, gasoline, and other fossil fuels [4, 5]. The primary sources for large-scale mono-alcohol production are sugarcane, switchgrass, maize,

* Corresponding author.
E-mail addresses: riteshphyzics@gmail.com, dr.riteshchaurasia@gmail.com (R.K. Chourasia).
[1] A constituent college of Lalit Narayan Mithila University, Darbhanga-846004, India.

https://doi.org/10.1016/j.heliyon.2022.e10532
Received 26 April 2022; Received in revised form 17 July 2022; Accepted 30 August 2022

natural gas, municipal trash, and coal [6]. The Worldwide fuel mandate [7] and also the expert committee on the roadmap for Ethanol blending in India by 2025 [8] is a viable method for promoting high-quality, standardized fuels on a global basis while simultaneously taking into account the necessity for maximum engine and vehicle endurance as well as the greenest feasible engine and vehicle technology operation. The execution of the targeted objectives will benefit consumers by streamlining fuel markets, stimulating the economy, and aiding governments in attaining their public policy goals.

Methanol and Ethanol are mono-alcohol hydrocarbons that are now sustainable and used as direct gasoline additives and as feedstock for the production of gasoline additives. Methanol and Ethanol have comparable physical-chemical properties, such as water solubility, density values, appearance, smell, and transparency [9]. The cheaper cost of water compared to mono-alcohols and their resemblance contribute to the simplicity with which hydrated mono-alcohol Fuels may be adulterated. The purity of high ethanol quality is critical to its long-term effectiveness as a fuel and a source of additional fuel additives. The information here includes manufacturer feedstock recommendations for the ethanol quality required for optimum engine and vehicle performance. The prescribed limits are for anhydrous 100 percent ethanol (E100) [10] blendstock intended to blend with petroleum-based gasoline to produce a maximum of 10% ethanol by volume (E10) appropriate for automobiles with spark-ignition engines. Higher-level mixes (more than E10) [11] are only suitable for use in vehicles designated for this type of fuel, such as “flexible propelled” cars, and Ethanol used for higher blends may have different restrictions. Ethanol is the most widely produced biofuel on the planet, with annual production reaching over 90 billion liters (yearly) in the previous decade. Such an energy matrix is a decent choice for petroleum derivatives in Europe, the United States, Brazil, Japan, India, Argentina, and Mexico. Anhydrous Ethanol is added to gasoline to increase fuel performance by acting as an octane stimulant [11]. The most common way to adulterate mono-alcohol fuel is to add too much water since the blends are translucent and have no distinctive fragrance. It results in a loss of power and an increased fuel consumption rate.

Additionally, the molar concentration of mono-alcohol changes significantly dependent on atmospheric temperature and varied meteorological circumstances [12, 13, 14, 15]. Because all-season types are common throughout India and the Asian continent, monitoring the molar content of contaminants in a binary composition of hydrated mono-alcohols in various weather situations should become a top focus. The physical properties of this pseudo-binary combination, such as refractive index, viscosity, and density, are all temperature-functional and connected [13, 14, 15]. As a result of the fluctuation in these parameters with temperature, the variation in the molar concentration of hydrated mono-alcohols during different climatic conditions must be felt. Infrared spectroscopy [16], indirect photometric determination [17], direct-injection enthalpimetry [18], cyclic voltammetry [19], photothermal detector [20], webcam photometer [21], ultrasonic propagation velocity [22] and surface plasmon sensor [23] have all been proposed for determining water content in mono-alcohol fuels. These approaches work well for mono-alcohols at static temperature behavior only. Given the likelihood of temperature-dependent molar concentrations of hydrated mono-alcohols adulteration, it is necessary to develop a quick, simple, and low-cost technique for detecting if the allowed maximum levels of these solvents have been exceeded with improved detection accuracy.

As a result, in contrast to the aforementioned investigations conducted in static surroundings and at static temperatures, the function of a temperature change as a result of variable climate/metrological circumstances is extended and included in our current research. Adulterant molar content in hydrated mono-alcohols is thus measured. For this task, we have used the hollow-core Bragg fiber (HCBF) with the defect layer as the sensing platform for the present analysis. As per our existing knowledge, this proposed work is entirely new and has been first accomplished and renowned using HCBF in the context of adulteration measures in mono-alcohols. The high and low RI periodic arrangement based concentric circular layer in length is the essential foundation of HCBF structure, where EM-wave is transmitted through the empty core under no. of Bragg reflections through the periodic claddings [24, 25, 30]. Under Bragg conditions, the HCBF structure also shows a photonic bandgap (PBG). A band of wavelengths known as the PBG range is not permitted to pass through the HCBF structure. HCBF has many encouraging applications in doubly tuned multi-wavelength LASER sources [26], biosensors [27], tunable voltage multiplexers [28], wavelength and intensity modulation [29, 30], etc. In this paper, the high RI contrast (e.g., chalcogenide glass Arsenic tri-selenide As_2Se_3 and polymer film Poly-ether imide PEI) and multi-clad HCBF structure has been investigated. The present hollow core in HCBF plays the role of an optofluidic flow cell for hydrated mono-alcohols throughout the sensing process. As we know, for transient response to improve the overall performance of sensing devices, narrow transmission bandwidth and constant intensity of output signal for inline application are needed. By inserting a PEI geometrical defect/flaw layer into the cladding periodicity and breaking the symmetry/creating asymmetry, it is possible to get this attribute in the present periodic structure. This layer is then used to produce a resonant transmission peak in the PBG area. With the aid of the TMT and mathematical HF formalism in a cylindrical coordinate system, the transmission characteristics of the electromagnetic (EM) wave through the under consideration HCBF structure were investigated.

The following is the proposed structure for the current communication: The detailed description of the HCBF structure and sensor device schematic layout using the Transfer matrix technique and Henkel formalism is provided in section 2. Section 3 addresses the results obtained, and Section 4 provides a summary conclusion.

2. Comprehensive outline of the HCBF structure and sensor device schematic setup

Fig. 1a shows the cladding RI and thickness profile of a pseudo-binary combination of water and mono-alcohols filled optofluidic core HCBF structure with a geometrical flaw. The longitudinal axis of the HCBF structure is cylindrically symmetric (propagation axis). The periodic repeating of bilayer high RI chalcogenide glassy substance Arsenic tri-Selenide As_2Se_3 (n_H, d_H) and low RI polymeric layer poly-ether-imide (PEI) creates the HCBF structure (n_L, d_L). Furthermore, by breaking the periodic arrangement’s symmetry, a low RI polymeric layer called poly-ether-imide (PEI) is imposed as a geometrical defect layer described by (n_D, d_D). Entirely thicknesses are chosen for maximum transmission intensity via a quarter-wave stack (QWS) condition of $n_H d_{H=} n_L d_L = n_D d_D = \lambda_0/4$, where λ_0 is the HCBF structure’s design wavelength. In addition, Fig. 1b shows the schematic configuration for optimizing the temperature-dependent molar concentration of the pseudo-binary combination of water and mono-alcohols using this HCBF adulteration sensor. The EM waves from the multi-wavelength broadband source impinge on the pseudo-binary mixture filled optofluidic core HCBF in this basic schematic configuration. After that, a photo-optic detector detects the output transmitted waves, then evaluates them by an optical spectrum analyzer on the computer setup.

2.1. Analytical modeling of HCBF structure: transfer matrix technique (TMT) and Henkel function (HF) formalism

Theoretical and mathematical modeling of the above-mentioned HCBF structure in cylindrical coordinates using TMM and Henkel formalism has been provided. The following is the refractive index profile of several layers of the HCBF structure used in this framework:

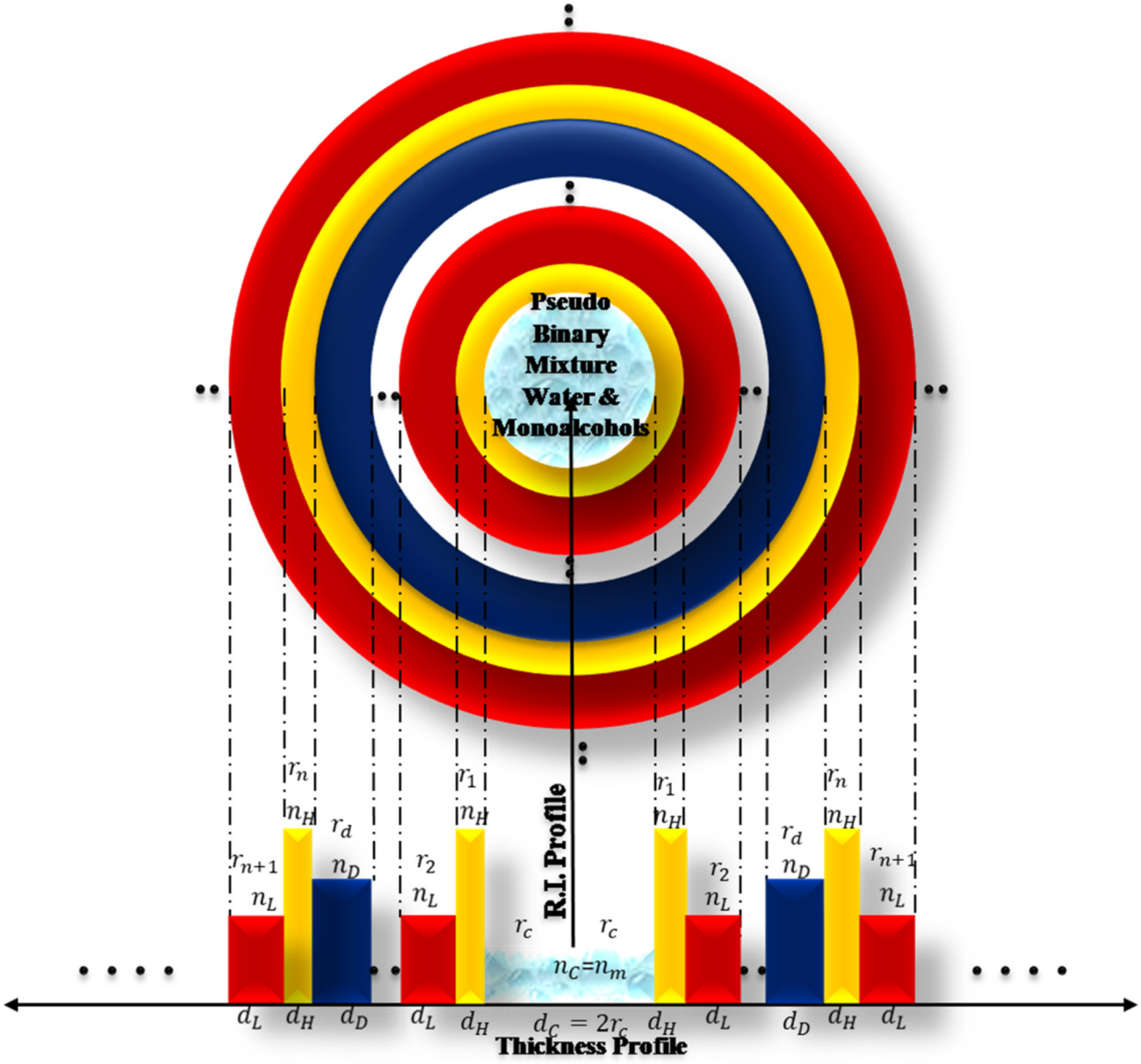

Fig. 1a. Thickness and RI profile of HCBF with geometrical defect layer and hydrated mono alcohols filled optofluidic core.

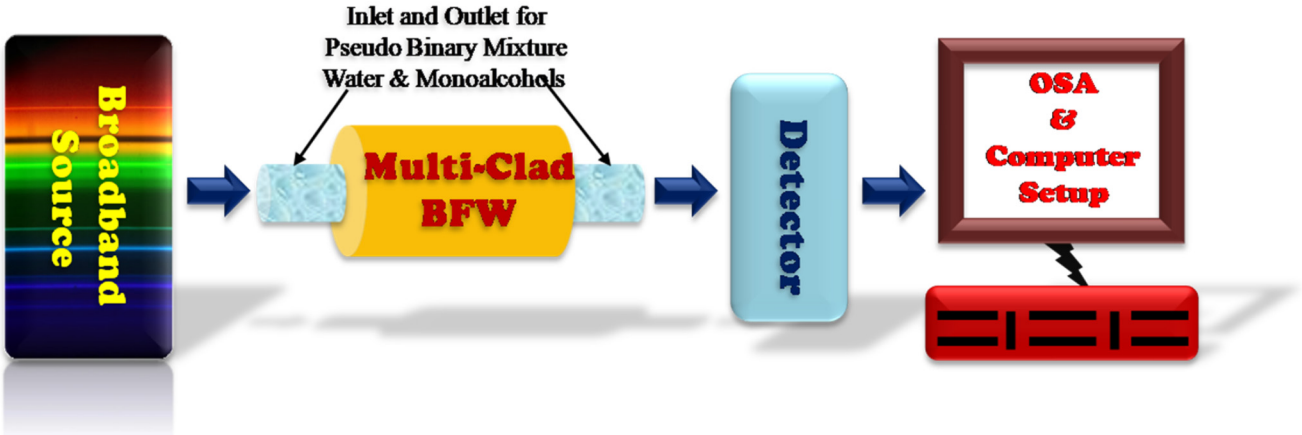

Fig. 1b. Schematic setup to optimize the temperature-functional concentration of adulterant in hydrated mono alcohols using HCBF adulteration optofluidic sensor device.

$$n(r)=\begin{cases} n_c, & 0\le r<r_c; \\ n_H, & r_c\le r<r_1; \\ n_L, & r_1\le r<r_2; \\ \vdots & \\ n_H, & r_{n-2}\le r<r_{n-1}; \\ n_L, & r_{n-1}\le r<r_D; \\ n_D, & r_D\le r<r_{D'}; \\ n_H, & r_{D'}\le r<r_{n+1}; \\ n_L, & r_{n+1}\le r<r_{n+2}; \\ \vdots & \\ \text{etc.} & \end{cases} \tag{1}$$

The cylindrical wave TMT [24, 25] may be used to create the above-specified HCBF structure solution to reflection and transmission. For a substrate with permeability μ and permittivity ϵ, the below Maxwell equations (2)-(3) [31, 32] are stated as:

$$\nabla \times E = -j\omega\mu H \tag{2}$$

$$\nabla \times H = j\omega\varepsilon E \tag{3}$$

The relationship among the longitudinal and transverse segments of the electric and magnetic fields is specified in the system of cylindrical co-ordinates (r, z) [31, 32], assuming that all fields have the same temporal aspect $exp(j\omega t)$. The Helmholtz wave equations (4)-(5) are expressed as follows in the cylindrical coordinate system [31, 32]:

$$r\frac{\partial}{\partial r}\left(r\frac{\partial H_z}{\partial r}\right)-r^2\frac{1}{\varepsilon}\frac{\partial \varepsilon}{\partial r}\frac{\partial H_z}{\partial r}+\frac{\partial}{\partial \theta}\left(\frac{\partial H_z}{\partial \theta}\right)+\omega^2\mu\varepsilon r^2 H_z=0 \ (TE\text{-mode}) \tag{4}$$

$$r\frac{\partial}{\partial r}\left(r\frac{\partial E_z}{\partial r}\right)-r^2\frac{1}{\mu}\frac{\partial \mu}{\partial r}\frac{\partial E_z}{\partial r}+\frac{\partial}{\partial \theta}\left(\frac{\partial E_z}{\partial \theta}\right)+\omega^2\mu\varepsilon r^2 E_z=0 \ (TM\text{-mode}) \tag{5}$$

The aforementioned differential equations may be solved using the variable segregation procedure. The Maxwell field solution is calculated for radial and angular components of the cylindrical wave [24, 31]. The TE-mode solution has three non-zero components (H_Z, E_θ, E_r), which are stated below in equations (6a), (6b) and (6c) [24]:

$$H_Z(r,\theta)=[AJ_m(kr)+BY_m(kr)]e^{jm\theta} \tag{6a}$$

$$E_\theta=\frac{1}{-j\omega\varepsilon}\frac{\partial H_z(r,\theta)}{\partial r} \tag{6b}$$

$$E_r=\frac{m}{\omega\varepsilon}\frac{H_z(r,\theta)}{r} \tag{6c}$$

where A and B are random constants and J_m are Y_m Bessel and Neumann functions, $k=\left(\frac{\omega}{c}\right)n$ is the wave vector of the medium, n represents the R.I. of the medium. The elements of the transfer matrix $\hat{T}$, that correlate the field vector to another point r from an initial position r_c are calculated using Abeles' multilayer structure theory [24, 32] and are described by the below equation (7) and (8) [24]:

$$\hat{T}=\begin{bmatrix} T_{11} & T_{12} \\ T_{21} & T_{22} \end{bmatrix} \tag{7}$$

$$T_{11}=\frac{\pi}{2}kr_c\left[Y'_m\left(kr_c\right)J_m(kr)-J'_m\left(kr_c\right)Y_m(kr)\right] \tag{8a}$$

$$T_{21}=j\frac{\pi}{2}kr_c p\left[Y'_m\left(kr_c\right)J'_m(kr)-J'_m\left(kr_c\right)Y'_m(kr)\right] \tag{8b}$$

$$T_{22}=\frac{\pi}{2}kr_c\left[J_m\left(kr_c\right)Y'_m(kr)-Y_m\left(kr_c\right)J'_m(kr)\right] \tag{8c}$$

$$T_{12}=-j\frac{\pi}{2}\frac{kr_c}{p}\left[J_m\left(kr_c\right)Y_m(kr)-Y_m\left(kr_c\right)J_m(kr)\right] \tag{8d}$$

where $p=\sqrt{\frac{\mu}{\varepsilon}}$ is the medium's intrinsic impedance. The asymmetric defect layer transfer matrix component must be written using the above-mentioned steps. Because the radii of two interfaces must be taken into account when calculating the element of the transfer matrix, the n^{th} transfer matrix $\hat{T}_n$, therefore, be determined by substituting $r_c \to r_{n-1}$, $r \to r_n$, $k \to k_n$ and $p \to p_n$. In addition, because the structure is periodic, we must take $n(r)=n_L$ if $n=$ even and $n(r)=n_H$ if $n=$ odd. We have total $(2N+1)$ layers in the HCBF structure with an asymmetric low RI defect layer; thus, the overall transfer matrix is written below in equation (9) [24]:

$$\begin{bmatrix} V(r_f) \\ U(r_f) \end{bmatrix}=T_{2N}.....T_2T_1\begin{bmatrix} V(r_c) \\ U(r_c) \end{bmatrix}=\hat{T}\begin{bmatrix} V(r_c) \\ U(r_c) \end{bmatrix} \tag{9}$$

$U(r)$ is the Helmholtz equation solution at point r, and $V(r)$ is the Helmholtz equation solution at point r. As shown above, transfer matrices, equivalent to Fresnel's equation [31] in a planar geometry, are used to compute propagation and wave reflection in a cylindrical structure with various layers. The reflection coefficient through the HCBF system could be calculated as below in equation (10) [31]:

$$r_M=\frac{(T'_{21}-jp_0c^{(2)}_{m0}T'_{11})+jp_fc^{(2)}_{mf}(T'_{22}-jp_0c^{(2)}_{m0}T'_{12})}{(-T'_{21}+jp_0c^{(1)}_{m0}T'_{11})+jp_fc^{(2)}_{mf}(-T'_{22}+jp_0c^{(1)}_{m0}T'_{12})} \tag{10}$$

In equation (10), the matrix element T'_{11}, T'_{22}, T'_{12} and T'_{21} are the inverse matrix element of matrix $\hat{T}$ in Eq. (9) and the below coefficient is given by equation (11) [31]

$$C^{(1,2)}_{ml}=\frac{H^{(1,2)'}_m(k_lr_l)}{H^{(1,2)}_m(k_lr_l)} \text{ with } l=0,\ f \tag{11}$$

For the azimuthal field variation m, the first and second kind Henkel function can be expressed by $H^{(1)}_m$ and $H^{(2)}_m$ respectively. The reflectance can be measured as $R=|r_M|^2$, and the percentage transmittance for non-absorbing media is calculated accordingly, $T=(1-R)\times 100$ with values between 0 to 100%. The TM-mode formula can be attained basically by inserting $\mu \leftrightarrow \varepsilon$ and $j \leftrightarrow -j$ it in the TE-mode expression.

2.2. The correlation between the RI of hydrated mono-alcohols with composition and temperature

Monoalcohals, whether pure or combined with water, are extensively used in a range of applications, with energy supply being our primary concern throughout the research. The surface tension, density, RI, viscosity, and other physical parameters of these pseudo-binary fuel resources are beneficial analytical information for fuel industries [13, 14, 15]. We are interested in two physical parameters, only RI and density, as per the need of our proposed sensor system. Therefore, the predictive capacity of different proposed equations Lorentz-Lorenz, Dale-Gladstone, Eykman, Newton, Kay, etc., has their strength. Still, the first two Lorentz-Lorenz and Dale-Gladstone have successfully explained the theoretical prediction and experimental matching [14]. The refractive index n_D and density ρ of a pseudo-binary mixture of mono-alcohols + water (hydrated mono-alcohols) also measured at a temperature of 298.15 K (room temperature) and atmospheric pressure. The refractive indices of these solutions have also been studied as a function of temperature in the range $T=278.15$ K to 323.15 K (desired range of weather temperature) and atmospheric pressure. The refractive indices acquired empirically and estimated using the Lorentz-Lorenz and Gladstone-Dale relations have been compared [14, 15]. The Gladstone-Dale equation yielded results that were similar to those observed experimentally in every case [14] for mono-alcohols. The excess molar volumes V^E and molar volume fraction deviations ΔR of these combinations, as well as the discrepancies between experimental and Gladstone-Dale RI values, have been calculated. Thus, the Lorentz-Lorenz relation below in equation (12) is the most widely used theoretical method for predicting the RI of pseudo-binary mixtures of liquids [14].

$$\frac{n_L^2-1}{n_L^2+2}=\emptyset_a\frac{n_{Da}^2-1}{n_{Da}^2+2}+\emptyset_b\frac{n_{Db}^2-1}{n_{Db}^2+2} \tag{12}$$

where n_L is the RI of the mixture according to the Lorentz-Lorenz formula; $\emptyset_a$ and $\emptyset_b$ are the molar fraction of hydrated mono-alcohols

Table 1a. Experimental measurements data of density (ρ) and mixture RIs (n_D) for Methanol (fuel) + Water pseudo-binary mixtures (hydrated mono-alcohol) along with the values obtained for n_G, n_L, Δn_G, ΔR and V^E at a temperature of 298.15 K [14].

S. No.	x	ρ (kg.m^{-3})	n_D	n_G	n_L	Δn_G	$\Delta R \times 10^{-6}$ (m^3.mol^{-1})	$V^E \times 10^{-6}$ (m^3.mol^{-1})
1	0.0000	997.02	1.3326	1.33260	1.33260	0.00000	0.00000	0.00000
2	0.3330	917.74	1.3396	1.34063	1.32931	−0.00103	−0.04050	−0.89700
3	0.6635	840.72	1.3360	1.33538	1.32737	0.00062	−0.01115	−0.84819
4	1.0000	786.62	1.3264	1.32637	1.32640	0.00000	0.00000	0.00000

Table 1b. Experimental measurements data of density (ρ) and mixture RIs (n_D) for Ethanol (fuel) + Water pseudo-binary mixtures (hydrated mono-alcohol) along with the values obtained for n_G, n_L, Δn_G, ΔR and V^E at a temperature of 298.15 K [14].

S. No.	x	ρ (kg.m^{-3})	n_D	n_G	n_L	Δn_G	$\Delta R \times 10^{-6}$ (m^3.mol^{-1})	$V^E \times 10^{-6}$ (m^3.mol^{-1})
1	0.0000	997.02	1.3326	1.33260	1.33261	0.00000	0.00000	0.00000
2	0.3332	894.81	1.3582	1.36071	1.34914	−0.00251	−0.06492	−1.02180
3	0.6664	825.77	1.3618	1.36111	1.35685	0.00069	−0.00134	−0.67725
4	1.0000	785.08	1.3593	1.35930	1.35892	0.00000	0.00000	0.00000

obtained from volume determinations based on mass and density measurements, n_{Da} and n_{Db} are the individual R.I.'s of the mono-alcohols and water, respectively. Empirical equations have also been established to determine the refractive indices of pseudo-binary liquid systems, including that proposed by Gladstone-Dale and represented below in equation (13) [14]:

$$\frac{n_G - 1}{\rho} = w_a \left(\frac{n_{Da} - 1}{\rho_a} \right) + w_b \left(\frac{n_{Db} - 1}{\rho_b} \right) \tag{13}$$

where n_G and ρ is the RI and experimental density of the mixture; w_a and w_b are the mass fraction of mono-alcohols and water; n_{Da} and n_{Db} are the again individual RIs of the mono-alcohols, and water, respectively. Several researchers have confirmed the validity of the Lorentz-Lorenz and Gladstone-Dale relationships in the context of various sorts of mixtures [13, 14, 15].

Calculations have been completed of the excess molar volume, V^E employing the following equation (14) [14]:

$$V^E = \frac{x_a M_a + x_b M_b}{\rho} - \frac{x_a M_a}{\rho_a} - \frac{x_b M_b}{\rho_b} \tag{14}$$

where ρ is the density of mixture; ρ_a and ρ_b are the density of the components; x_a and x_b are the respective molar fractions, M_a and M_b are the molar masses of the pure components.

Further, the molar refraction deviations, ΔR to optimize the accuracy of the measurements, have been calculated from the following expressions (15) and (16) [14]:

$$R_m = \left(\frac{n_D^2 - 1}{n_D^2 + 2} \right) \frac{x_a M_a + x_b M_b}{\rho} \tag{15}$$

$$\Delta R = R_m - (x_a R_{a+} x_b R_b) \tag{16}$$

where n_D is the RI of the mixture. In contrast, calculations have also been made of the differences between RIs obtained experimentally, n_D and that calculated from the equation of Gladstone-Dale, n_G i.e. $\Delta n_G = n_D - n_G$.

2.3. HCBF optofluidic adulteration sensor performance parameter

In this work, the performance of the proposed HCBF optofluidic adulteration concentration sensor is assessed using its performance parameters, sensitivity (S), detection accuracy (DA), and overall quality parameter (QP). The ratio of the measured output to the variation in the physical quantity being monitored is known as the sensor's sensitivity. Therefore, the sensitivity of the current sensor is theoretically defined as the ratio of a spectral shift in resonance wavelength to a minute change in analyte RI or molar concentration.

$$S = \Delta\lambda_{res}/\Delta n_a \quad \text{or,} \quad S = \Delta\lambda_{res}/\Delta\left(V_a/V\right) \tag{17}$$

where $\Delta\lambda_{res}$ is the change in resonant sensing signal wavelength and Δn_a is the change in RI in hydrated medium, V_a is the volume fraction of mono-alcohol in water, and 'V' is the volume of a pseudo-binary mixture. The detection accuracy (DA) parameter, which describes the true value of the measurand, is also crucial. The ratio of change in resonant sensing signal wavelength to the FWHM of the resonant sensing signal is the DA of this sensor.

$$D.A. = \Delta\lambda_{res}/\Delta\lambda_{0.5} \tag{18}$$

where $\Delta\lambda_{0.5}$ is spectral width at 50% of transmittance. The quality parameter (QP) is another important performance parameter that demonstrates the overall performance of the presented sensor with an important sensitivity parameter, and DA QP is defined as:

$$Q.P. = S/\Delta\lambda_{0.5} \tag{19}$$

where S is known as sensitivity defined in Eq. (17) and $\Delta\lambda_{0.5}$ is the FWHM of the sensing signal. According to the results of the study, the FWHM of the sensing signal should be as narrow as feasible to minimize the inaccuracy in identifying the sensing signal wavelength.

3. Numerical findings and discussion

The HCBF optofluidic fuel sensor with a geometrical flaw is designed, theoretically modeled, and further compared with some other published results to optimize the adulterants in temperature-functional concentration of hydrated mono-alcohols (Methanol and Ethanol) fuel. The current sensor arrangement is based on the EM wave's design wavelength $\lambda_0 = 1550$ nm. The core of Bragg fiber is hollow enough that it may function as an optofluidic flow cell and store a pseudo-binary mixture of hydrated mono-alcohols. The hollow core's circumference is kept large enough to easily retain the mixture. Furthermore, the core is encircled by concentric cladding layers of Arsenic tri-selenide, a high RI material As_2Se_3 ($n_H = 2.82$) and low RI material Poly-ether-imide PEI ($n_L = 1.66$) [24, 25] with their thicknesses followed by a quarter-wave stack (QWS) condition $n_H d_H = n_L d_L = n_D d_D = \lambda_0/4$. Furthermore, a low-index material defect layer (Poly-ether-imide) with RI ($n_D = 1.66$) and QWS thickness $d_D = \lambda_0/4n_d$ is introduced in the mid of periodic stacking ($N = 16$) by breaking the symmetry, i.e., creating asymmetry in the periodicity of concentric cladding layers. The glass/polymer combination was chosen in this investigation for the ease of production of HCBF. The polymer PEI has good thermal stability up to 400 °C [33] with glass transition temperature above 220 °C in the visible and near-infrared region, which is necessary for additional monitoring of the temperature-dependent (present temperature study range is 5 °C-50 °C only) transmission spectra. The achieved results of this study have been shown in Table 3a and Table 3b and further plotted in Fig. 4 and Fig. 5. The performance of the present device is tabulated in Table 4. Since the

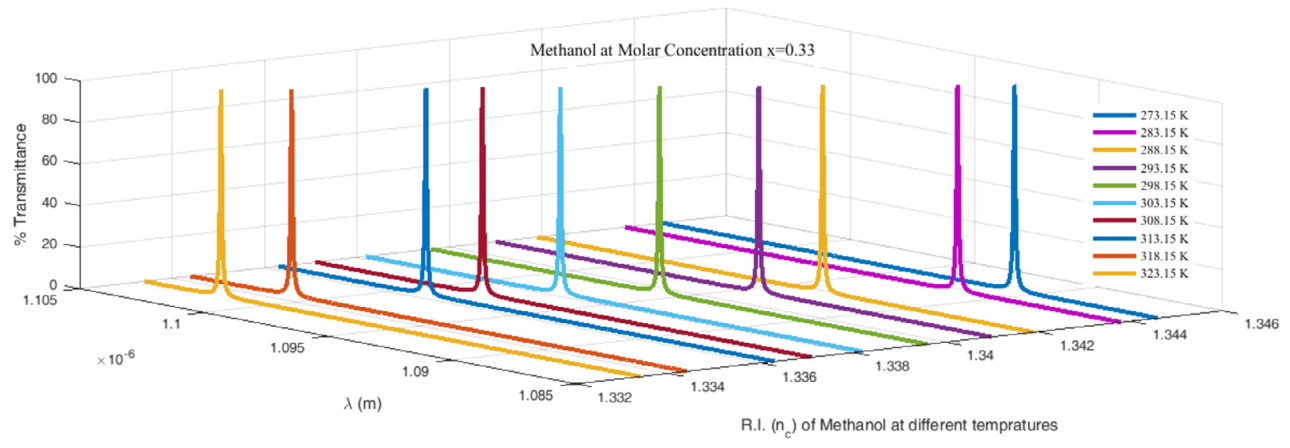

(a)

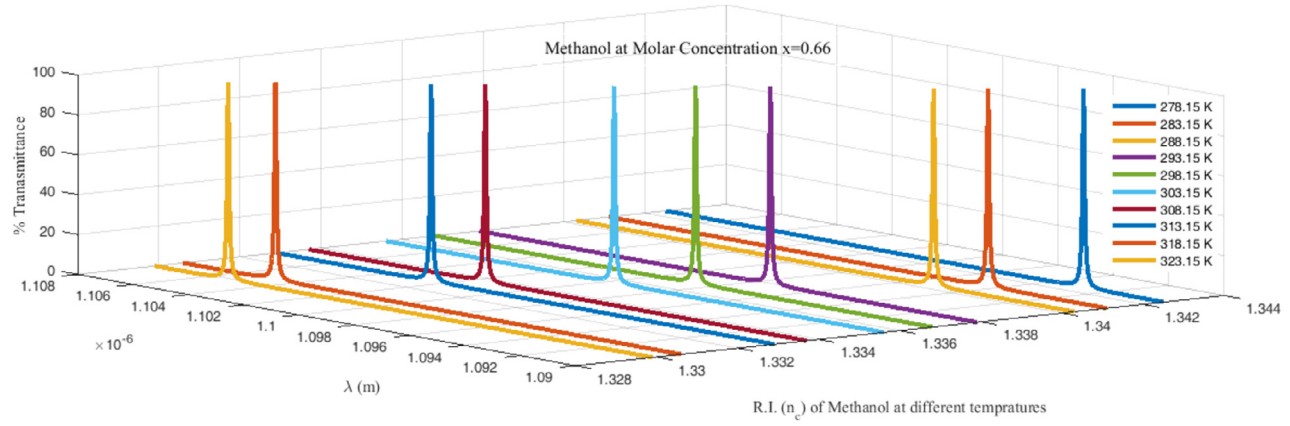

(b)

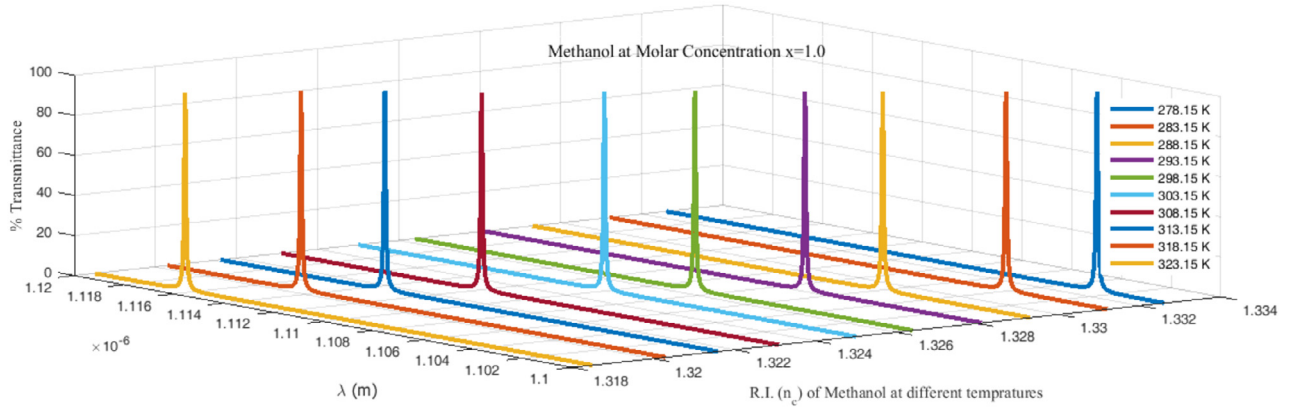

(c)

Fig. 2. Finding sensing signal position for the different fractions of hydrated Methanol fuel at various temperatures by using HCBF spectrum.

temperature (due to different weather conditions and temperature variation throughout the day) has superior significance in the present study, therefore in Fig. 2a, 2b, 2c, and Fig. 3a, 3b, 3c, the PBG along with sensing signal peak positions have been estimated through transmittance spectra for Methanol and Ethanol in pseudo-binary hydrated fuel at temperatures of interest. The above transmission spectra have been drawn using equations (10)-(11) and Tables 1a-1b and 2. The obtained sensing signal peak positions at different temperatures (5 °C-50 °C) for all three molar fractions ($x = 0.33$, 0.66, and 1.00) have been optimized in Table 3a and 3b. These sensing signal peaks having the least FWHM of about 0.1 nm only are necessary for sensing applications.

The findings also indicate that the sensing signal exhibits an effective redshift with the smallest FWHM of 0.1 nm for various molar fractions at various temperatures, which will be used to enhance a performance parameter for the HCBF sensor that has a geometrical fault. Figs. 4 and 5 depict the relationships between the sensing signal peak wavelength and different molar percentage fractions of methanol and ethanol in the applicable temperature range. This study displays the lin-

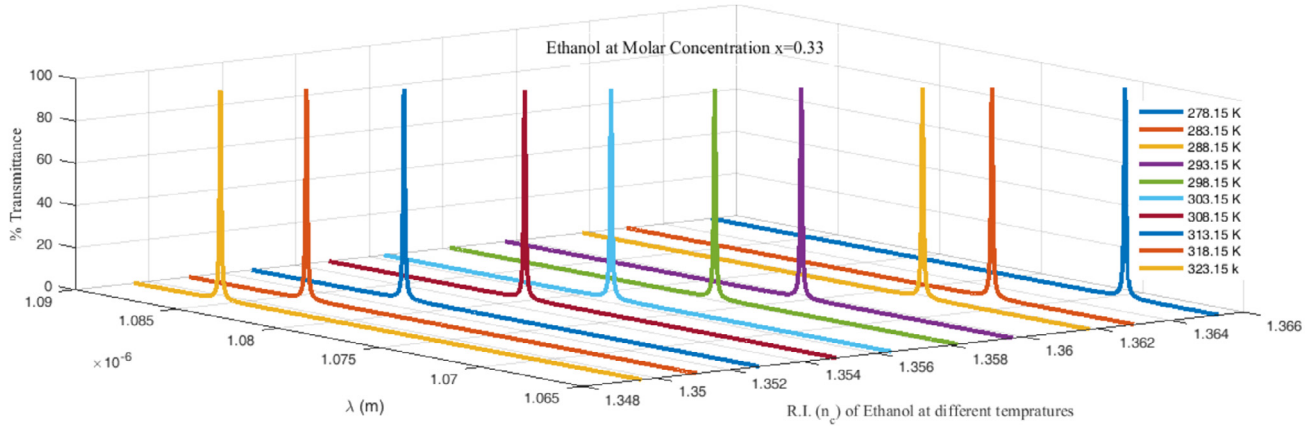

(a)

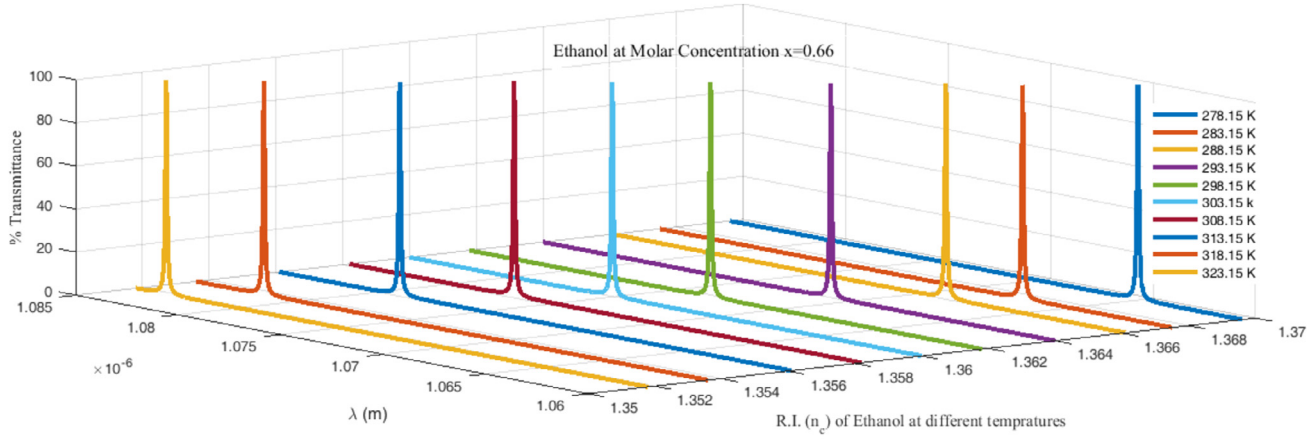

(b)

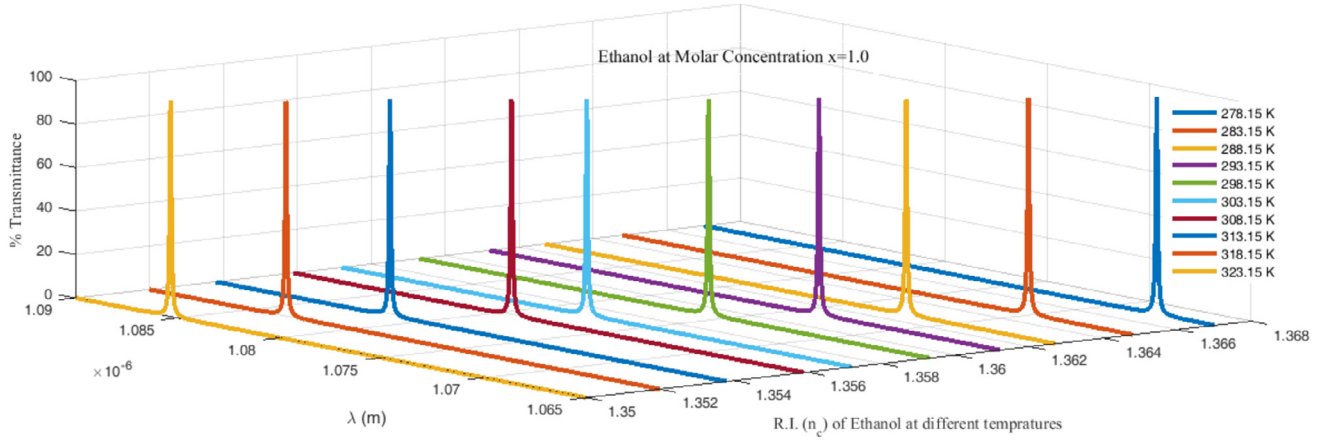

(c)

Fig. 3. Finding sensing signal position for the different fractions of hydrated Ethanol fuel at various temperatures by using HCBF spectrum.

ear signature of variation between the peak wavelength of the sensing signal and various molar fractions at different weather temperatures. As constant sensitivity is preferred for high sensor performance, which is tabulated in Table 4 and displayed in Fig. 6, this linear variation will result in the outstanding performance of the suggested sensor. A comparative performance analysis for the mono-alcohols is plotted in Fig. 6.

From Table 4 and Fig. 6, it is clear that the maximum found sensitivity is 1057.3 nm/RIU in the case of ethanol fuel rather than methanol fuel. Further, we compared the obtained results with the static temperature molar concentration measurement of adulterants in hydrated mono-alcohol fuel using a surface plasmon resonance optic sensor recently published by Kumar et al. [23]. Our obtained result is superior

Table 2. The RI variations with the temperature of the soluble mono-alcohol fuel for each of the specified molar fractions (x).

S. No.	T (K)	Methanol (x) + Water			Ethanol (x) + Water		
		$x = 0.33$	$x = 0.66$	$x = 1.0$	$x = 0.33$	$x = 0.66$	$x = 1.0$
1.	**278.15**	1.3446	1.3425	1.3326	1.3653	1.3696	1.3670
2.	**283.15**	1.3438	1.3411	1.3312	1.3630	1.3675	1.3648
3.	**288.15**	1.3419	1.3403	1.3293	1.3618	1.3661	1.3627
4.	**293.15**	1.3410	1.3379	1.3281	1.3527	1.3640	1.3612
5.	**298.15**	1.3396	1.3368	1.3264	1.3582	1.3618	1.3593
6.	**303.15**	1.3382	1.3356	1.3250	1.3564	1.3600	1.3572
7.	**308.15**	1.3371	1.3337	1.3231	1.3549	1.3582	1.3559
8.	**313.15**	1.3363	1.3329	1.3216	1.3528	1.3561	1.3538
9.	**318.15**	1.3344	1.3306	1.3203	1.3511	1.3536	1.3520
10.	**323.15**	1.3334	1.3299	1.3185	1.3496	1.3518	1.3500

Table 3a. Sensing signal position measurement for the various molar fraction of Methanol at different temperatures.

S. No.	T (K)	Methanol ($x = 0.33$)		Methanol ($x = 0.66$)		Methanol ($x = 1.0$)	
		R.I.	Sensing signal (nm)	R.I.	Sensing signal (nm)	R.I.	Sensing signal (nm)
1	**278.15**	1.3446	1092.00	1.3425	1093.01	1.3326	1103.01
2	**283.15**	1.3438	1092.04	1.3411	1094.04	1.3312	1104.04
3	**288.15**	1.3419	1093.08	1.3403	1095.01	1.3293	1106.00
4	**293.15**	1.3410	1094.05	1.3379	1097.09	1.3281	1107.05
5	**298.15**	1.3396	1096.00	1.3368	1099.08	1.3264	1109.01
6	**303.15**	1.3382	1097.04	1.3356	1100.02	1.3250	1110.04
7	**308.15**	1.3371	1098.05	1.3337	1102.02	1.3231	1112.02
8	**313.15**	1.3363	1099.03	1.3329	1103.00	1.3216	1113.04
9	**318.15**	1.3344	1101.09	1.3306	1104.03	1.3203	1115.02
10	**323.15**	1.3334	1103.00	1.3299	1105.01	1.3185	1116.04

Table 3b. Sensing signal position measurement for the various molar fraction of Ethanol at different temperatures.

S. No.	T (K)	Ethanol ($x = 0.33$)		Ethanol ($x = 0.66$)		Ethanol ($x = 1.0$)	
		R.I.	Sensing signal (nm)	R.I.	Sensing signal (nm)	R.I.	Sensing signal (nm)
1	**278.15**	1.3653	1070.01	1.3696	1065.06	1.3670	1068.01
2	**283.15**	1.3630	1072.02	1.3675	1067.04	1.3648	1070.04
3	**288.15**	1.3618	1073.01	1.3661	1069.00	1.3627	1072.01
4	**293.15**	1.3597	1075.03	1.3640	1071.01	1.3612	1074.05
5	**298.15**	1.3582	1077.05	1.3618	1073.03	1.3593	1076.03
6	**303.15**	1.3564	1079.04	1.3600	1075.00	1.3572	1078.04
7	**308.15**	1.3549	1081.01	1.3582	1077.01	1.3559	1079.05
8	**313.15**	1.3528	1082.09	1.3561	1079.02	1.3538	1081.02
9	**318.15**	1.3511	1084.06	1.3536	1082.08	1.3520	1083.01
10	**323.15**	1.3496	1086.07	1.3518	1084.01	1.3500	1085.04

to their achieved result in terms of sensitivity and practical difficulties in the realization of the surface plasmon sensor. Thus the HCBF optofluidic adulteration sensor may play a good role in optimizing adulterants in a temperature-dependent molar fraction of hydrated mono-alcohols. Furthermore, the other sensing performance parameters as QP and DA, which are firmly inversely proportional to the FWHM of sensing signal (Eq. (18) and Eq. (19)), appear best in result in comparison to the result obtained in [23] because the least FWHM value of sensing signal peak in the present study. To the best of our knowledge, we are the first to present this type of optic sensor with a better performance parameter, which is also more convenient and accessible than those now available.

4. Conclusion

An HCBF optofluidic adulteration sensor with a geometrical flaw has been effectively developed in the current communication for optimizing and monitoring the adulterants in a temperature-dependent molar percentage of hydrated mono alcohols Fuel in various weather conditions. A narrow sensing transmission peak is obtained in the measured PBG due to a geometrical flaw in the HCBF structure, which is sensitive enough to changes in the hydrated fuel-filled core RI. The performance metrics of the current optofluidic sensor are substantially improved as compared to other similar sensors due to the smallest FWHM of the sensing signal. The maximum achieved a sensitivity of the HCBF sensor is 1057.3 nm/RIU in all weather conditions, which is superior to the attained sensitivity for surface plasmon resonance optic sensor for concurrent sensing of hydrated mono-alcohols but at static temperature. Because the other sensing performance metrics DA and QP are inversely proportional to the obtained FWHM of the sensing signal peak, the least FWHM for this structure improves these sensing characteristics as well.

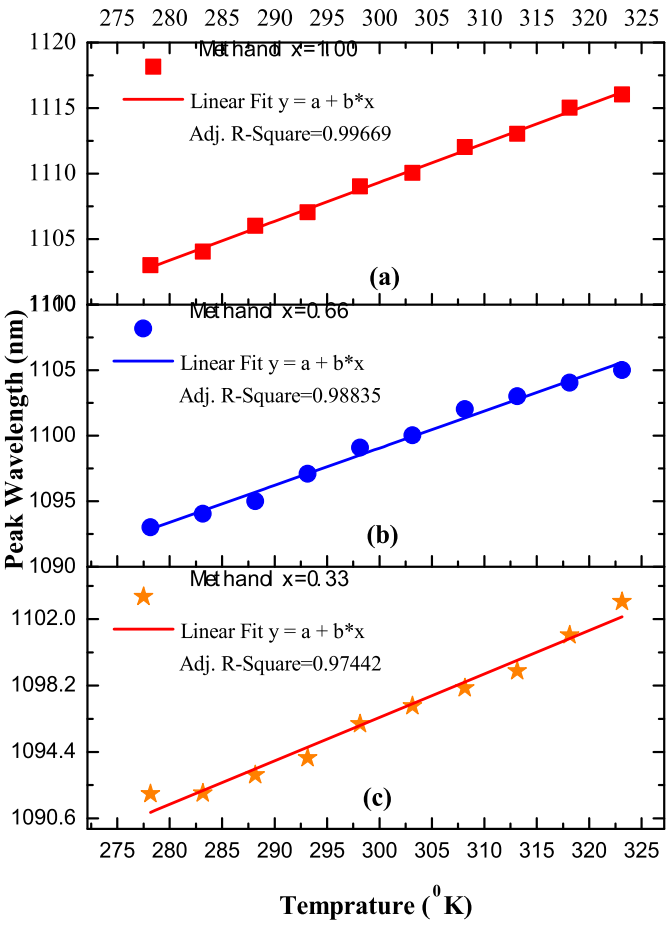

Fig. 4. Representation of sensing signal vs. temperature at a different concentration of Methanol in binary hydrated fuel.

Declarations

Author contribution statement

Dr. Nitesh Kumar Chourasia: Conceived and designed the experiments Analyzed and interpreted the data; Wrote the paper.

Mr. Narendra Bihari: Performed the experiments; Contributed reagents, materials, analysis tools or data.

Dr. Ritesh Kumar Chourasia: Conceived and designed the experiments Analyzed and interpreted the data; Contributed reagents, materials, analysis tools or data; Wrote the paper.

Funding statement

This research did not receive any specific grant from funding agencies in the public, commercial, or not-for-profit sectors.

Table 4. Sensing performance parameters estimation of HCBF optofluidic adulteration sensor for optimizing the temperature-functional concentration of mono alcohols in hydrated binary fuel mixtures.

Average sensing parameters	Methanol			Ethanol		
	$x = 0.33$	$x = 0.66$	$x = 1.00$	$x = 0.33$	$x = 0.66$	$x = 1.00$
Sensitivity (S) (nm/RIU)	982.14	952.38	943.26	1057.32	1039.32	1017.65
Detection Accuracy (D.A.)	110.0	120.0	133.0	166.0	185.0	173.0
Q.P. (RIU^{-1})	9.82×10^3	9.52×10^3	9.43×10^3	1.05×10^4	1.03×10^4	1.01×10^4

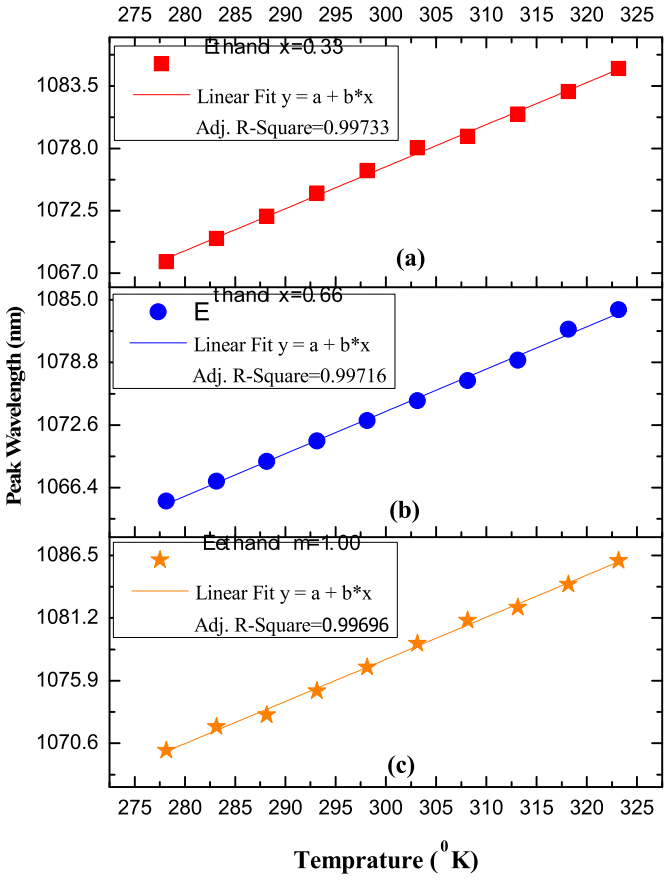

Fig. 5. Signature of sensing signal vs. temperature at various concentrations of Ethanol in binary hydrated fuel.

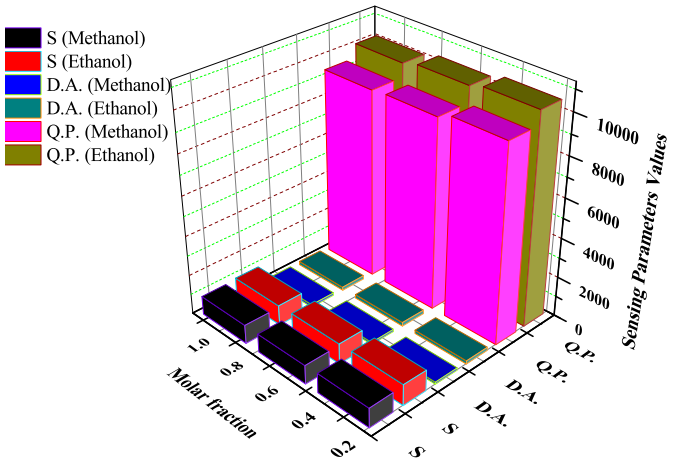

Fig. 6. Representation of sensing performance metrics of proposed HCBF optofluidic adulteration sensor.

Data availability statement

Data will be made available on request.

Declaration of interests statement

The authors declare no conflict of interest.

Additional information

No additional information is available for this paper.

References

[1] C. Sayin, Engine performance and exhaust gas emissions of methanol and ethanol–diesel blends, Fuel 89 (2010) 3410–3415.
[2] D.C. Rakopoulos, C.D. Rakopoulos, D.T. Hountalas, E.C. Kakaras, E.G. Giakoumis, R.G. Papagiannakis, Investigation of the performance and emissions of bus engine operating on butanol/diesel fuel blends, Fuel 89 (10) (2010) 2781–2790.
[3] Erdiwansyah, R. Mamat, M.S.M. Sani, K. Sudhakar, Asep Kadarohman, R.E. Sardjono, An overview of Higher alcohol and biodiesel as alternative fuels in engines, Energy Rep. 5 (2019) 467–479.
[4] Omar I. Awad, R. Mamat, Obed M. Ali, N.A.C. Sidik, T. Yusaf, K. Kadirgama, Maurice Kettner, Alcohol and ether as alternative fuels in spark ignition engine: a review, Renew. Sustain. Energy Rev. 82 (3) (2018) 2586–2605.
[5] Meisam Ahmadi Ghadikolaei, Chun Shun Cheung, Ka-Fu Yung, Study of combustion, performance, and emissions of a diesel engine fueled with diesel/biodiesel/alcohol blends having the same oxygen concentration, Energy 157 (2018) 258–269.
[6] Y.N. Guragain, K.V. Probst, P.V. Vadlani, Fuel Alcohol Production, second edition, in: Colin Wrigley, Harold Corke, Koushik Seetharaman, Jon Faubion (Eds.), Encyclopedia of Food Grains, Academic Press, 2016, pp. 235–244.
[7] IEA, Renewables 2021, IEA, Paris, 2021, https://www.iea.org/reports/renewables-2021.
[8] https://www.niti.gov.in/expert-committee-roadmap-ethanol-blending-india-2025.
[9] N.P. Cheremisinoff, Industrial Solvents Handbook, 2nd ed., Marcel Dekker, New York, 2003.
[10] L. Li, Z. Liu, H. Wang, B. Deng, et al., Combustion and Emissions of Ethanol Fuel (E100) in a Small SI Engine, SAE Technical Paper 2003-01-3262, 2003, https://doi.org/10.4271/2003-01-3262.
[11] Mengzhu Zhang, Yunshan Ge, Xin Wang, Daisy Thomas, Sheng Su, Hu Li, An assessment of how bio-E10 will impact the vehicle-related ozone contamination in China, Energy Rep. 6 (2020) 572–581.
[12] R.J. Jiménez Riobóo, M. Philipp, M.A. Ramos, et al., Concentration and temperature dependence of the refractive index of ethanol-water mixtures: influence of intermolecular interactions, Eur. Phys. J. E 30 (2009) 19.
[13] Nur Aainaa Syahirah Ramli, Fadzlina Abdullah, Study of density, surface tension, and refractive index of binary mixtures containing alkyl levulinate and n-alcohol from 298.15 to 323.15 K, J. Chem. Eng. Data 66 (5) (2021) 1856–1876.
[14] J.V. Herráez, R. Belda, Refractive indices, densities and excess molar volumes of monoalcohols + water, J. Solution Chem. 35 (2006) 1315–1328.
[15] Juan Ortega, Densities and refractive indices of pure alcohols as a function of temperature, J. Chem. Eng. Data 27 (3) (1982) 312–317.
[16] Adenilton Camilo Silva, Liliana Fátima Bezerra Lira Pontes, Maria Fernanda Pimentel, Márcio José Coelho Pontes, Detection of adulteration in hydrated ethyl alcohol fuel using infrared spectroscopy and supervised pattern recognition methods, Talanta 93 (2012) 129–134.
[17] Gabriela Furlan Giordano, Danielle Cristhina Melo Ferreira, Thiago Ribeiro de Carvalho, Luis Carlos Silveira Vieira, Maria Helena de Oliveira Piazzetta, Renato Sousa Lima, Angelo Luiz Gobbia, Portable platform for rapid and indirect photometric determination of water in ethanol fuel samples, Anal. Methods 6 (23) (2014) 9497–9502.
[18] W.A. De Oliveira, C. Pasquini, Determination of water in ethanol and acetone by direct injection enthalpimetry based on the heat of dilution, Talanta 31 (1984) 82.
[19] P.F. Pereira, R.M.F. Sousa, R.A.A. Munoz, E.M. Richter, Simultaneous determination of ethanol and methanol in fuel ethanol using cyclic voltammetry, Fuel 103 (2013) 725.
[20] Cleidson R. Omido, Samuel L. Oliveira, Juliete R. Lima, Keurison F. Magalhães, Aparecido A. de Carvalho, Cláudio Kitano, Water content in hydrated ethanol fuel measured by a photothermal chamber with a transparent transducer, Fuel 157 (1) (2015) 122–125.

[21] Hebertty V. Dantas, Mayara F. Barbosa, Anderson Pereira, Márcio J.C. Pontes, Pablo N.T. Moreira, Mário C.U. Araújo, An inexpensive NIR LED Webcam photometer for detection of adulterations in hydrated ethyl alcohol fuel, Microchem. J. 135 (2017) 148–152.
[22] M.K.K. Figueiredo, R.P.B. Costa-Felix, L.E. Maggi, A.V. Alvarenga, G.A. Romeiro, Biofuel ethanol adulteration detection using an ultrasonic measurement method, Fuel 91 (2012) 209.
[23] S. Kumar, G. Sharma, V. Singh, Modeling of surface plasmon resonance sensor for detection of mass concentration of ethanol and methanol in a binary mixture, Infrared Phys. Technol. 67 (2014) 190–196.
[24] R.K. Chourasia, V. Singh, Estimation of photonic bandgap in the hollow core cylindrical multilayer structure, Superlattices Microstruct. 116 (2018) 191–199.
[25] R.K. Chourasia, S. Prasad, V. Singh, Performance study of a liquid-core Bragg fiber sensor in the presence of a defect layer, Opto-Electron. Rev. 25 (2017) 215–221.
[26] N.K. Chourasia, A. Srivastava, V. Kumar, R.K. Chourasia, Doubly electrically tuned cylindrical Bragg fiber waveguide inline optical filter for multi-wavelength LASER applications, Mater. Today Commun. 25 (2020) 101620.
[27] R.K. Chourasia, C.S. Yadav, A. Upadhyay, N.K. Chourasia, V. Singh, Analysis of Bragg fiber waveguides having a defect layer for biosensing application, Optik 200 (2020) 163400.
[28] R.K. Chourasia, S. Prasad, V. Singh, Voltage-tunable passband in a cylindrical multilayered structure containing PMMA and 0.67 PMN–0.33 PT single crystal as a defect layer, Opt. Quantum Electron. 48 (12) (2016) 539.
[29] R.K. Chourasia, C.S. Yadav, A. Upadhyay, N.K. Chourasia, V. Singh, Comparative study of defect mode intensity and wavelength modulation in Bragg fiber waveguide sensors, Optik (2020) 164198.
[30] N.K. Chourasia, A. Srivastava, V. Kumar, R.K. Chourasia, Optimizing temperature-dependent molar volume fraction of biodiesel fuel in a pseudo-binary mixture through Bragg fiber waveguide sensor having defect layer, Fuel 293 (2021) 120489.
[31] M. Born, E. Wolf, Principles of Optics, Cambridge University Press, London, 1999.
[32] A.W. Snyder, J. Love, Optical Waveguide Theory, 2nd ed., Springer, 2008.
[33] Ramil Mercado, Yubao Wang, Tony Flaim, William DiMenna, Udayan Senapati, Thin-film polyetherimides with controlled refractive indices, in: Proceedings of SPIE: Organic Photonic Materials and Devices VI, 2004, p. 5351.